Composites Part B 200 (2020) 108358

Contents lists available at ScienceDirect

Composites Part B

journal homepage: www.elsevier.com/locate/compositesb

Strengthening mechanism and micropillar analysis of high-strength NiTi–Nb eutectic-type alloy prepared by laser powder bed fusion

Shifeng Liu [a,b,1], Song Han [a,b,1], Ling Zhang [c,d], Liang-Yu Chen [e], Liqiang Wang [a,*], Liang Zhang [c], Yujin Tang [f,**], Jia Liu [f], Huiping Tang [b], Lai-Chang Zhang [g,***]

[a] State Key Laboratory of Metal Matrix Composites, School of Material Science and Engineering, Shanghai Jiao Tong University, No. 800 Dongchuan Road, Shanghai, 200240, China
[b] School of Metallurgical Engineering, Xi'an University of Architecture and Technology, No.13 Yanta Road, Xi'an, 710055, China
[c] International Joint Laboratory for Light Alloys (MOE), College of Materials Science and Engineering, Chongqing University, Chongqing, 400045, China
[d] Electron Microscopy Center of Chongqing University, Chongqing University, Chongqing, 400044, PR China
[e] School of Materials Science and Engineering, Jiangsu University of Science and Technology, Mengxi Road 2#, Zhenjiang, 212003, PR China
[f] Affiliated Hospital of Youjiang Medical University for Nationalities, Baise, Guangxi, 533000, China
[g] School of Engineering, Edith Cowan University, 270 Joondalup Drive, Joondalup, Perth, WA, 6027, Australia

ARTICLE INFO

Keywords:
Laser powder bed fusion
Eutectic phase
Heat treatment
Strengthening mechanism
Micropillar compression

ABSTRACT

Although laser powder bed fusion (LPBF) can produce complex structures with promising properties, there still exists a concern on the diversity in materials, especially composites, for LPBF. This work innovatively used NiTi and Nb powders to prepare NiTi–Nb eutectic-type alloy by LPBF, which provides a new method to prepare NiTi–Nb shape memory alloy and could be an alternative for tailoring microstructure. The semi-molten Nb particle phase was retained during LPBF, so that β-Nb and the eutectic structure display a gradient distribution in the Nb diffusion concentration. The heat treatment process (annealed at 850 °C for 0.5 h) makes NiTi–Nb samples have high yield strength (~1640 MPa), high compressive strength (~2380 MPa), and high compressive strain (~39%), which are superior to the corresponding ones of its as-built and as-cast counterparts. Large Nb phase particles with a size of 10–30 μm are retained and accelerated the formation of eutectic phase and β-Nb precipitate phase. Overall, the presence of β-Nb phase has a beneficial effect on the alloy, and a large number of intertwined dislocations and stacking faults around the β-Nb phase promote the formation of martensite under stress loading. The eutectic phase makes an important contribution to the high strength and plasticity of the NiTi–Nb alloy.

1. Introduction

NiTi alloys, as the most important type of shape memory alloys (SMA) with unique superelasticity and shape memory effect, have attracted considerable interest for potential applications in aerospace and biomedical fields [1,2]. Compared with other SMAs, such as iron-based and copper-based alloys, NiTi-based SMA materials typically exhibit high strength and plasticity, good corrosion resistance, and excellent biocompatibility, making them a promising type of materials for biomedical applications [3]. However, brittle second phases are commonly observed in NiTi alloys, such as the most brittle metastable Ni_4Ti_3 phase which can gradually decompose into Ni_3Ti_2 and Ni_3Ti with increasing temperature and time [4]. Brittle second phase enhances the hardness but unfortunately reduces both the toughness and ductility of NiTi alloys [5,6]. Therefore, there is a significant need to effectively introduce second phases with high strength into NiTi matrix.

It is known that Nb plays an important role in NiTi–Nb alloys because Nb addition increases the transition hysteresis of NiTi alloys [7,8]. Furthermore, the bioavailability of Nb promotes the biocompatibility of NiTi-based alloys [9–11]. In previous work, NiTi–Nb eutectic alloy was prepared by sintering or casting to solve the above problems, and most of them have focused on their microstructure evolution and mechanical

* Corresponding author.
** Corresponding author.
*** Corresponding author.
E-mail addresses: wang_liqiang@sjtu.edu.cn (L. Wang), tangyujin196709@163.com (Y. Tang), l.zhang@ecu.edu.au, lczhangimr@gmail.com (L.-C. Zhang).
[1] The authors contribute equally.

https://doi.org/10.1016/j.compositesb.2020.108358
Received 16 June 2020; Received in revised form 7 August 2020; Accepted 10 August 2020
Available online 14 August 2020
1359-8368/© 2020 Elsevier Ltd. All rights reserved.

properties [7,12,13]. For example, Fan et al. [12] investigated the as-cast NiTi–Nb alloys with different Ni/Ti ratios and indicated a large number of Nb-rich particles (30–50 nm) uniformly precipitated into NiTi matrix and β-Nb particles with diameter of 200–300 nm in the eutectic region. The β-Nb particles can hinder martensitic transformation and reduce the martensite start temperature (M_s). Phase transformation mechanisms of NiTi–Nb alloys were also revealed [8,14]. For instances, dislocation slipping, stress-induced B19′ martensite phase transformation, and deformation twins were previously reported in a eutectic NiTi–Nb alloy [8]. Wang and his collaborators [4,8,14] studied the microstructure evolution and superelastic properties of the eutectic region in porous NiTi–Nb and observed that a large number of dislocations and stacking faults presented between the β-Nb phase and the eutectic phase. The dislocations and stacking faults accelerate the eutectic phase transformation. Nb element could not completely dissolve into the NiTi matrix and eutectic phase would appear when the Nb content is higher than 5.0 at.% [15]. Nb atoms replace the Ti atoms in the NiTi matrix and reduce the shear modulus of NiTi-rich phase, which facilitates the occurrence of martensite phase [16].

Until now, most as cast or sintered NiTi–Nb components have been limited by structure, shape and forming time. Thus, it is necessary to develop novel NiTi–Nb preparation methods to optimize microstructural features and mechanical properties for broad applications. Laser powder bed fusion (LPBF) is a relatively mature additive manufacturing process that uses a focused high-energy laser beam to selectively melt the deposited powder bed layer by layer [17–20]. Compared with traditional subtractive manufacturing methods (that is, removing excessive parts from the base ingot by rolling, cutting, etc.), the microscaled melt pools melted by laser have high temperature and ultra-fast cooling (10^5–10^6 K/s) [21]. LPBF has been demonstrated to be capable to manufacture a variety of metals such as stainless steels [5,22,23], aluminum alloys [24,25], and titanium alloys [26,27]. In addition, studies of NiTi shape memory alloys produced by LPBF have also been carried out [28], which focused on the effects of processing parameters on the microstructure evolution and mechanical properties of NiTi. Yang et al. [29] studied the effect of laser beam energy density on the microstructure of NiTi and found that high energy suppresses the formation of the B19′ martensitic phase and stabilizes the B2 austenitic phase. The instantaneous reaction in the LPBF process could significantly affect the microstructure of a material. In general, the rapid solidification of the micro-pool is accompanied by the formation of equiaxed and columnar crystals [30]. However, LPBF technology may introduce new defects such as cracks or pores during the preparation process, which may lead to unsatisfactory mechanical properties, thus limiting practical applications [30]. Heat treatment is an effective way to reduce defects and re-homogenize a microstructure [31]. In addition, samples prepared by LPBF often have more dislocations, and the original dislocations work with dislocations induced under stress, thereby enhancing the strength of an alloy [32].

LPBF-produced titanium-based materials have been studied by numerous researchers, focusing on the understanding of microstructural design, processing optimization, and mechanical performance. Zhang et al. [33] successfully prepared titanium-copper alloy with equiaxed fine-gained microstructure by fusion-based metal additive manufacturing, and determined the relationship of the solidification pathway and grain size. Todaro et al. [34] proposed to refine grains by controlling solidification paths using high-intensity ultrasound and found that this method could significantly promote the transformation of coarse grains into fine equiaxed grains. According to the NiTi-based alloy system, uneven distribution of chemical composition and the specific temperature field of LPBF are closely related to phase transition and microstructural features [35]. Overall, there remains insufficient understanding on the microstructure evolution and deformation mechanism of LPBF-produced NiTi–Nb SMAs.

Currently, using pre-alloyed powder has been proven to make the LPBF-fabricated components with more homogenous microstructure and stable mechanical properties. However, the preparation of pre-alloyed powder is usually cost- and time-consuming. In comparison, using powder mixture for LPBF is more economical and time-saving. Powder mixture has become a promising method to overcome the drawbacks of using pre-alloyed powders in LPBF process [32,36–39]. Fischer et al. [36] directly melted the non-spherical Ti and Nb powder mixture by laser beam and prepared a homogeneous alloy, which showed that the non-spherical shape has no obstacle to achieve homogeneity and high density. Kang et al. [37,38] adopted LPBF to prepare alloy samples from different powder mixtures and they have obtained hypereutectic Al–Si alloys and Ti–Mo alloys with high relative density. However, because the laser micro-region in the LPBF process is sintered and cooled rapidly, there is insufficient time for the alloying element to diffuse and reach a homogeneous state. Therefore, chemical inhomogeneity is obtained by sometimes un-melted or partially melted particles from those elements with high melting point in the microstructure. For example, Wang et al. [32] prepared Ti–35Nb alloy (wt.%) using element powder mixture by LPBF technology and found undissolved Nb particles in the Ti–35Nb alloy. The initiation sites of the slip bands are easily generated at the boundary of large Nb particles. They also showed that heat treatment could improve the chemical uniformity and microstructure uniformity, thereby making the microstructure more uniform and the Nb particles smaller.

To the best of the authors' knowledge, the preparation, microstructure, and properties of NiTi–Nb ternary alloys prepared by LPBF are still not well understood. In this work, NiTi pre-alloyed spherical powder was blended with a small amount of irregular Nb powder to prepare NiTi–Nb eutectic-type alloy by LPBF. This work focuses on the contributions of eutectic phase and Nb element to the mechanical properties and microstructure evolution of LPBF-produced NiTi–Nb eutectic alloy. Uniaxial compression was performed to compare the mechanical properties of NiTi–Nb alloys in different states. Additionally, the mechanical behavior and deformation mechanism of the eutectic phase and the Nb-rich phase were compared using micropillar compression experiment. The lattice interface of Nb-rich phase and NiTi matrix in the eutectic microcolumn region was investigated by transmission electron microscopy (TEM) imaging with focusing ion beam (FIB). This work reveals a comprehensive understanding of the strengthening mechanism and phase transformation characteristics of NiTi–Nb eutectic-type alloy with high performance.

2. Experimental

2.1. Sample preparation

The quasi-binary eutectic NiTi–Nb phase diagram in Fig. 1 (a) shows that the eutectic composition is $Ni_{38}Ti_{36}Nb_{26}$ (at.%) [40]. Fig. 1 (b) schematically shows the raw material powders including pre-alloyed spherical NiTi (50.0 at.% Ni) powder and non-spherical pure Nb powder. As shown in Fig. 1 (c), the pre-alloyed NiTi powder and Nb powder (at a weight ratio of 4:1) were mixed and blended for 1 h. The nominal chemical composition of blended powder was $Ni_{44}Ti_{44}Nb_{12}$ (at.%), and Nb content is greater than 10 at.%, which ensures that Nb and NiTi can form eutectic phases above the eutectic temperature [40]. All the samples were produced using an FS271 M LPBF machine (Farsoon High-Technology, China), equipped with a 500 W fiber laser and operated in continuous mode at a 70–200 μm spot in an argon gas environment. As shown in Fig. 1 (d), the processing parameters were set as follows: laser power was 200 W, powder layer thickness was 30 μm, laser spot size was 120 μm, and laser scanning speed was 600 mm/s. The direction of scanning was rotated through 67° between successive layers. The substrate was pre-heated to 160 °C to reduce the difference in temperature between the first layer and the substrate and to avoid the partial separation of the sample from the substrate (due to warping effect) [41].

The samples prepared by LPBF were removed from the substrate by

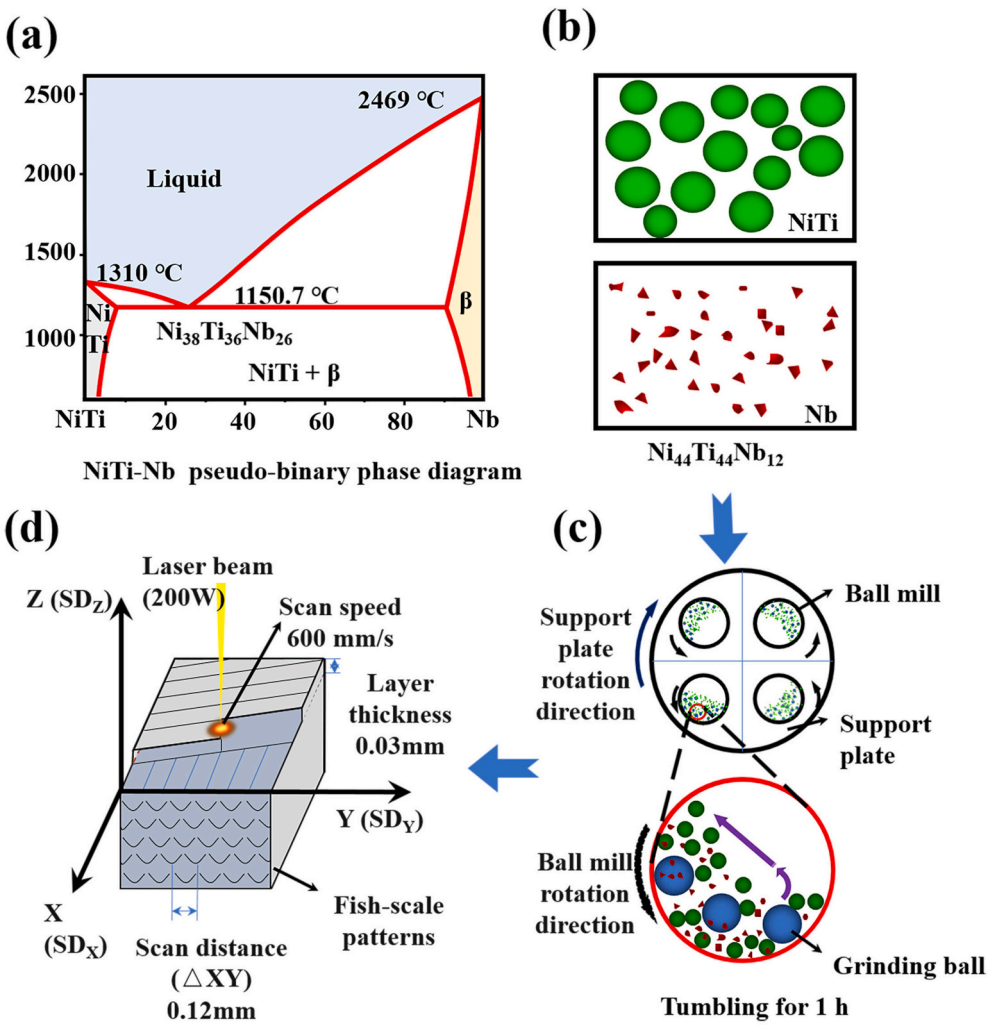

Fig. 1. Schematic illustrating NiTi–Nb preparation: (a) pseudo-binary phase diagram of NiTi–Nb system [40], (b) the NiTi and Nb powder, (c) powder mixing process diagram, (d) schematic for the processing parameters in LPBF.

wire electric discharge machining. Then, samples were annealed in an argon atmosphere at 850 °C (above the recrystallization temperature), and then maintained in a furnace for 0.5 h. The sample preparation and heat treatment parameters were optimized according to a large number of literature focusing on the process parameters and annealing treatment of LPBFed NiTi alloy [42–44]. The density of the NiTi–Nb was measured as 6.62 g/cm^3 (relative density ≥ 99.5%) using the Archimedes method.

2.2. Uniaxial compression

The mechanical properties of the samples were assessed through compression test on an MTS servo-hydraulic machine. Cyclic loading-unloading compression was carried out both on the as-built and the annealed samples of dimensions Φ4 × 6 mm. The applied cyclic compressive strains were 3%, 6%, 9%, 12%, 15%, 18%, and 21%, respectively. All samples were compressed at a loading rate of 0.1 mm/min at room temperature. Compression were performed following GB/T 7314-2017.

2.3. Micropillar compression

The micropillar was fabricated by focusing ion beam using Scios DualBeam. The current range was controlled at 15–0.1 nA, and was gradually reduced to match the micropillar dimensional accuracy of the layer-by-layer peeling. The FIB was used to remove material around the pillar, stripping to a micropillar with a height of ~6 μm and a diameter of ~2 μm, ensuring ~3:1 aspect ratio for micropillar compression [6]. Micropillar compression was performed under displacement-controlled mode using a Zeiss Auriga SEM-FIB equipped with a Hysitron PI88 system. Load-displacement data was continuously recorded during the tests. A constant 5 nm/s compression rate was maintained during compression with a maximum displacement of ~2000 nm.

2.4. Microstructural observation

Differential scanning calorimetry (DSC) was used to characterize the phase transformation temperatures by DSC 200 F3 in a temperature range of -150-100 ℃, with heating and cooling rates of 10 ℃/min. The samples were ground and polished to a mirror finish by standard metallographic procedures, and etched by reagent (composed of ~10 vol% HNO_3, 20 vol% HF, and 70 vol% H_2O) for ~ 15 s. The phase composition was determined by X-ray diffraction (XRD) using a Regaku D/max 2200pc diffractometer. The XRD radiation source was Cu-Kα and the angle range was 30–80°. The etched sections were imaged by optical microscopy (Nikon MA200 Eclipse) and scanning electron microscopy (SEM, Hitachi 8030). The microstructure of the compressed sample was characterized by transmission electron microscopy (TEM), and high resolution TEM (HRTEM) using a JEOL 2100F with 200 kV voltage at room temperature. TEM specimens were sampled from the compressed fracture zone and prepared by twin-jet polishing in a solution with 3 vol

% perchloric acid and 97 vol% alcohol at −25 °C.

3. Results

3.1. Microstructure characteristics

Fig. 2 (a) shows the SEM microstructure of the mixed NiTi–Nb powder. The blended powder includes the pre-alloyed spherical NiTi powder and the non-spherical pure Nb powder, with particle sizes of 10–50 μm and 5–30 μm in diameter, respectively. The actual chemical composition of the mixed powder is $Ni_{43.8}Ti_{44.0}Nb_{12.2}$ (at. %). Fig. 2 (b) shows the XRD results of NiTi–Nb mixed powder, as-built, and annealed samples. The mixed powder based on XRD pattern shows mainly B2 austenite phase and β-Nb phase. The as-built and annealed samples are also mainly composed of B2 phase and β-Nb phase. It is well known that annealing treatment can eliminate residual stress in LPBF-prepared samples, uniform tissue composition and refine grains [31]. The β-Nb phase in NiTi–Nb alloy further precipitated during the annealed process, which hindered the growth of austenite grains. The large number of small austenite grains with irregularly arranged crystal planes is the reason why the intensity of the B2 diffraction peak in the XRD results is lower than that of the prepared sample.

Fig. 3 shows the optical microstructures of the as-built and the annealed samples. A laser scanning pitch of ~120 μm and a consecutive two-layer angle of 67° are clearly visible in the morphology of the XY cross-section for the as-built samples (Fig. 3 (a)). The microstructure of the XZ cross-section of the as-built sample (Fig. 3 (b)) reveals that some "fish scale" like tracks are formed with the continuous layer-by-layer accumulation of micro-molten pools. The approximate height and width of the fan-shaped molten pool in the XZ section are 30 μm and 130 μm, respectively. Some Nb particles with 10–20 μm in diameter accumulate at the bottom of molten pool boundaries. This is caused by the powder flow during powder deposition process. Due to the relatively small size and high gravity, Nb particles tend to locate at the bottom of the molt pool.

As indicated by the red dashed lines in the X-Z section of the sample (Fig. 3 (c)), the boundaries of the laser scanning paths of the sample (with width of about 120 μm) becomes blurred after annealing, and some incompletely melted Nb-rich particles are observed. The same scenario is observed at interfaces between the molten pools in the X-Z section, with apparent diffusion paths as indicated by the red dashed lines on Fig. 3 (d). Almost no pores and cracks are observed in all samples, demonstrating that LPBF can effectively facilitate formation of the NiTi–Nb eutectic-type alloy. Fig. 3 (e) shows an enlarged view of the X–Y cross-section of the laser path. Two kinds of crystalline grains with large difference in sizes are observed at the boundaries and in the interior of tracks. The enlarged X-Z cross-section of the laser path (Fig. 3 (f)) shows that the trajectory boundaries are with a large number of small equiaxed grains (200 nm - 2 μm in size). The grains in the central part are mainly composed of large columnar grains, about 10 μm wide and 40 μm long. The equiaxed grains are uniform and fine in size, and they are distributed at the molten pool boundaries; by contrast, the coarse columnar grains are solidified toward the center of molten pool due to thermal gradient.

Fig. 4 shows the SEM morphology of the as-built NiTi–Nb eutectic-type alloy manufactured by LPBF. The morphology of the Nb particles (~20 μm) and the diffusion of Nb elements around the Nb particles are shown in Fig. 4 (a). In addition to the Nb particles, β-Nb precipitates are found at the grain boundaries in the eutectic region, as shown in Fig. 4 (b). Submicron β-Nb (~300 nm) is distributed with a lamellar shape in the triangular grain boundary as seen in the enlarged view of the grain boundary (Fig. 4 (c)). This microstructure was reported previously in Ref. [45]. The number of Nb precipitates at the grain boundaries increases significantly with the increase in the Nb content [45]. Fig. 4 (d) shows the eutectic microstructure of the Nb particles. The distribution of the eutectic phases in the molten region is relatively uniform. The molten layer consists of a rod-shaped primary NiTi–Nb phase near Nb particles, and a large number of rod-like eutectic phases and lamellar β-Nb phases can be seen in the enlarged image (Fig. 4 (e)). Based on the NiTi–Nb binary pseudo-eutectic phase diagram [40], a NiTi–Nb eutectic liquid phase is formed when the melting temperature reaches the eutectic temperature [16].

As seen from the TEM image in the eutectic region of the annealed sample (Fig. 5 (a)), the annealed sample is mainly composed of submicron-sized Nb-rich phase precipitating in NiTi matrix. The selected area electron diffraction (SAED) pattern of the β-Nb phase and NiTi (B2) (Fig. 5 (b)) illustrates that the Nb and NiTi phases have two coincident crystal planes (100) and (011) planes. Thus, the crystal planes corresponding to the two planes are parallel to each other, with an orientation relationship of $(100)_{β\text{-Nb}}//(011)_{B2}$ and $[01\bar{1}]_{β\text{-Nb}}//[01\bar{1}]_{B2}$. A high-resolution TEM image (Fig. 5 (c)) of the area (Fig. 5 (a)) shows that the distance between the atoms near the Nb-rich phase is 0.275 nm and the atomic distance close to the NiTi (the family plane) is 0.270 nm. In addition, there are severe lattice distortions between the atoms in the red dashed area shown in Fig. 5 (c), which is mainly attributed to the disorder in atom arrangement. The dislocation structures formed during additive manufacturing are shown in Fig. 5 (d). Compared with the traditional preparation method, the transient micro-melt pool of the LPBF process induces more severe internal lattice distortion, dislocations, and residual stress [41]. In general, as-LPBFed samples exhibit high strength but poor toughness, thus post-processing treatment such as annealing and aging is required to balance the strength and toughness [46].

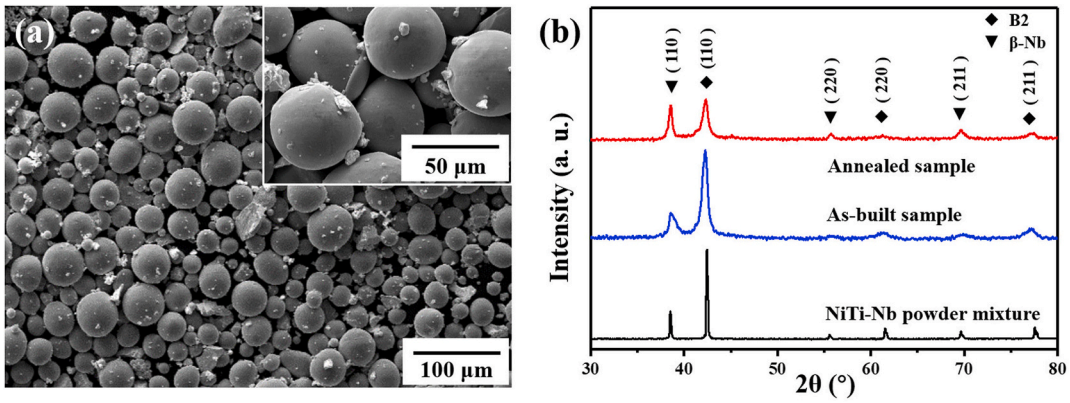

Fig. 2. (a) SEM images of the NiTi–Nb powder and (b) XRD patterns of the NiTi–Nb mixed powder, as-built sample, and its annealed counterpart.

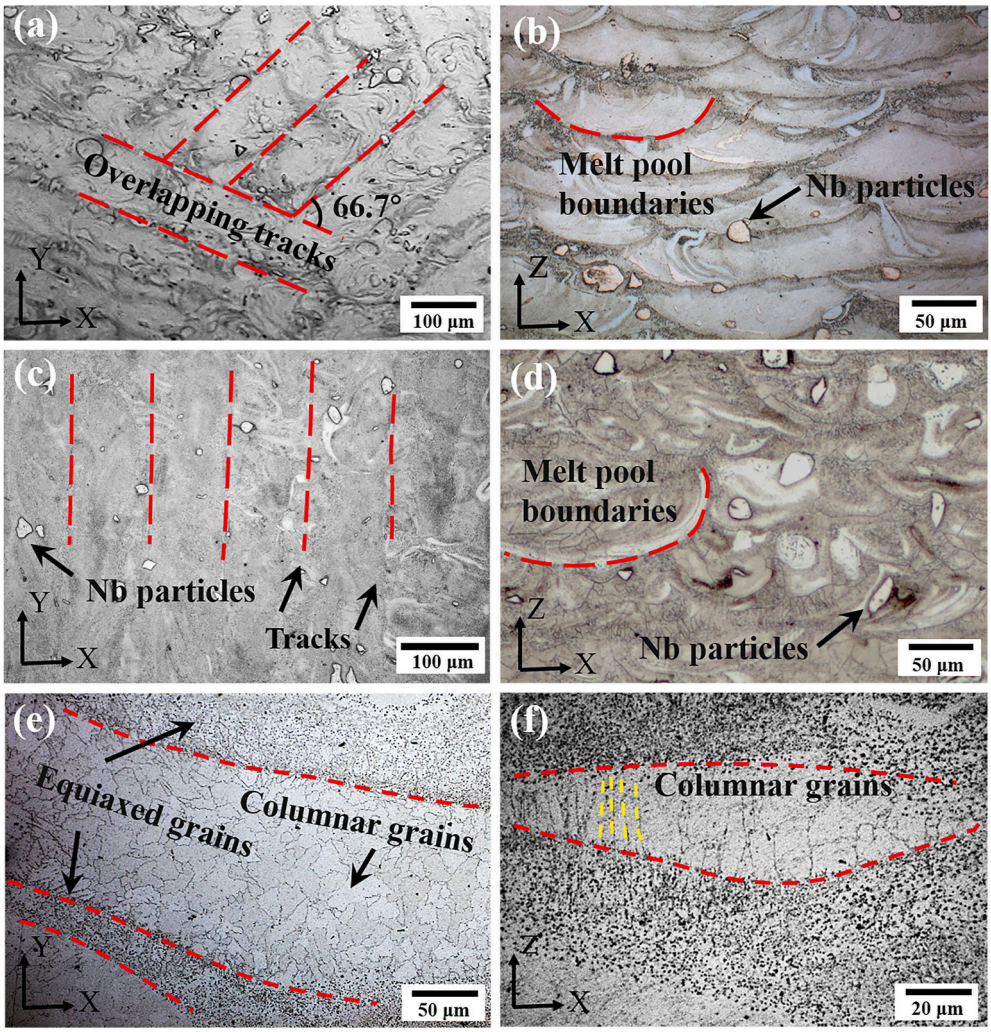

Fig. 3. Optical microstructures of: (a) XY cross-section from the as-built NiTi–Nb, (b) XZ cross-section from the as-built NiTi–Nb, (c) XY cross-section from the annealed NiTi–Nb, (d) XZ cross-section from the annealed NiTi–Nb, (e) enlarged view of the XY cross-section, (f) enlarged view of the XZ cross-section.

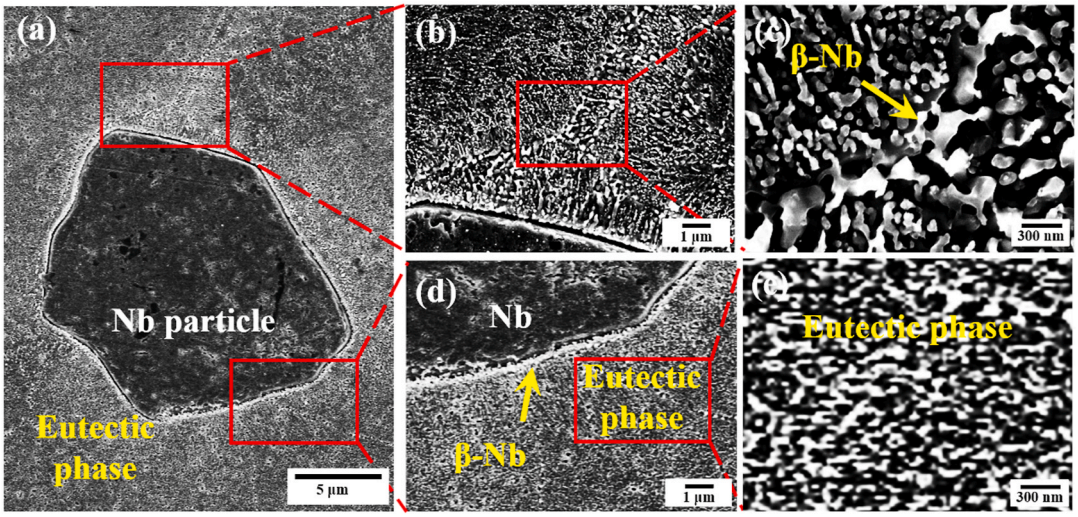

Fig. 4. SEM images showing the microstructure of the as-built NiTi–Nb manufactured by LPBF: (a) surrounding morphology of semi-melted Nb particles, (b) magnified area around the grain boundary, (c) magnified area indicated in (b), (d) microstructure of another area near the Nb particle, (e) the eutectic region.

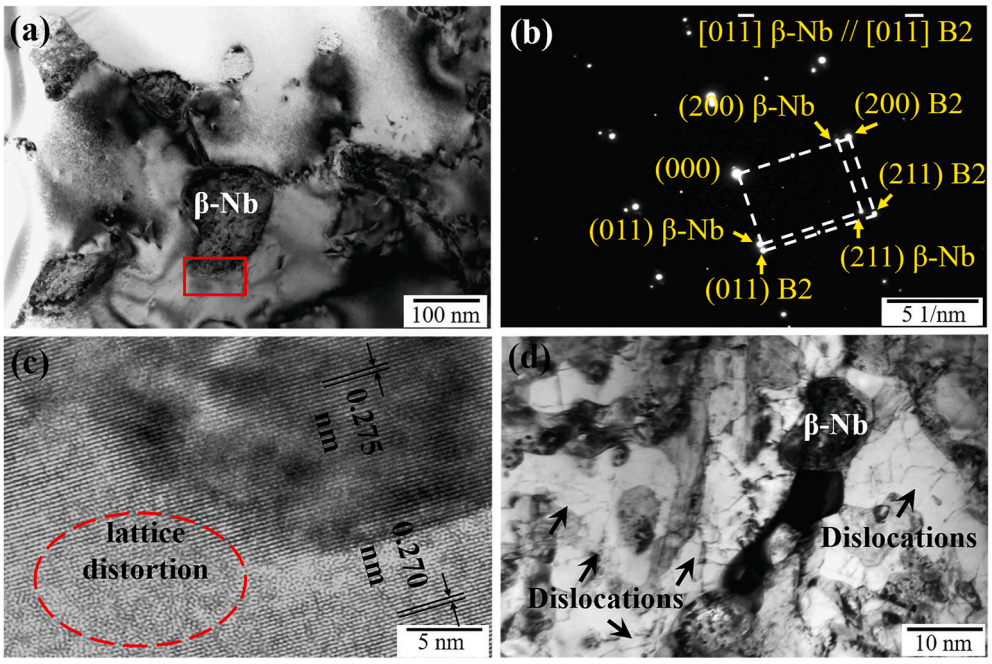

Fig. 5. (a) TEM micrograph of the eutectic region in the annealed sample manufactured by LPBF, (b) The selected area electron diffraction pattern of the β-Nb phase and NiTi, (c) a high-resolution image of the indicated area in (a), and (d) the dislocation structures formed in the annealed sample.

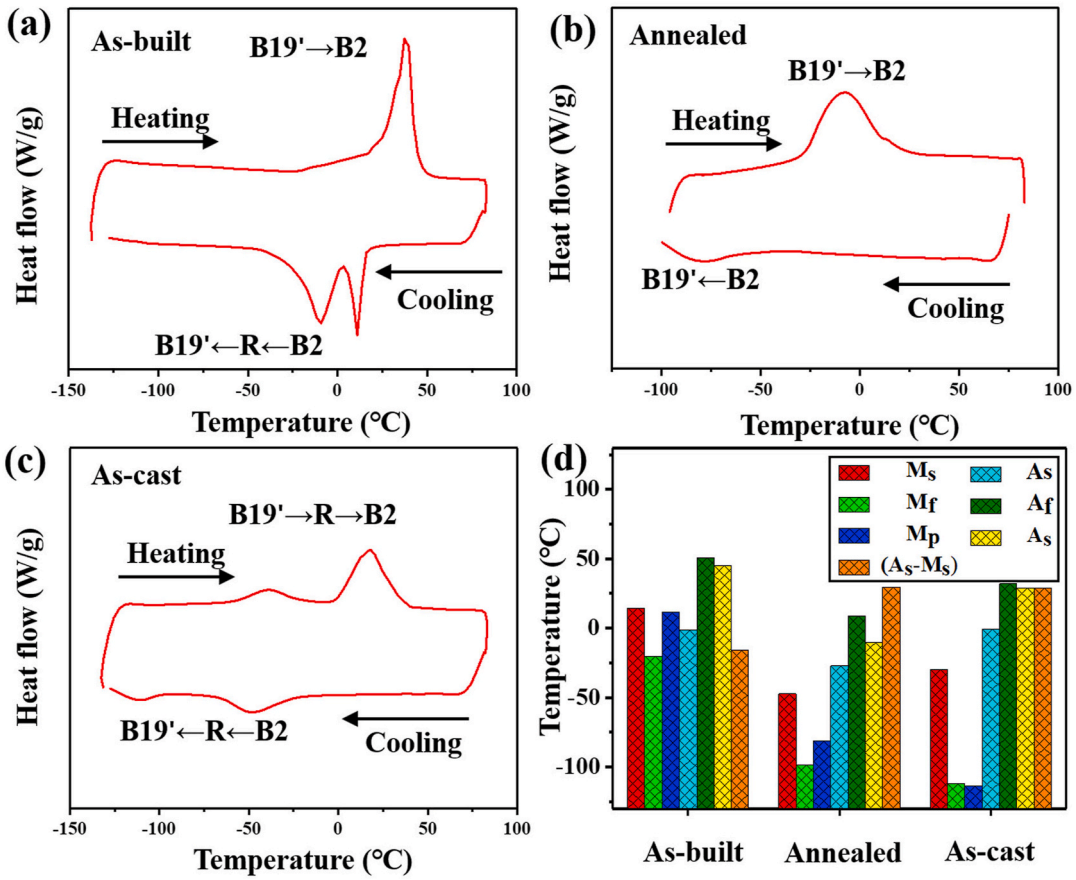

Fig. 6. DSC curves of NiTi–Nb samples: (a) as-built NiTi–Nb; (b) annealed sample; (c) as-cast sample; (d) the variation of several key characteristic temperatures. M_s: martensite start temperature; M_f: martensite finish temperature; M_p: martensite peak temperature; A_s: reverse martensite start temperature; A_f: reverse martensitic finish temperature; A_p: reverse martensite peak temperature.

3.2. Phase transformation

Fig. 6 (a) shows the DSC curves and phase transformation temperatures for the as-built $Ni_{44}Ti_{44}Nb_{12}$. The as-built sample demonstrates a single-stage B19'→B2 transformation in the heating stage, and a two-stage B2→R→ B19′ transformation during cooling, where R transformation is an intermediate phase [8,14]. The samples annealed at 850 °C display a single-stage phase transformation, with no R phase transformation in both heating and cooling stages, as shown in Fig. 6 (b). The as-cast counterpart with the same composition reveals a distinct secondary phase transformation feature in both heating and cooling: B19'→R→B2 and B2→R→B19' (Fig. 6 (c)). The M_s value for near-equiatomic NiTi alloy is approximately from 50 to 100 °C [16]. All characteristic temperatures are shown in Fig. 6 (d) and summarized in Table 1. Compared with the as-built sample produced by LPBF, the annealed sample shows lower transformation temperatures for martensite and austenite, with an average temperature drop by about 54 °C. In addition to the increase in M_f, the M_s, A_s, and A_f of the annealed sample decrease slightly compared to the as-built counterparts. The transition hysteresis (A_s-Ms) was determined to be −15.9 °C, 29.6 °C, and 29.0 °C for as-built, annealed, and as-cast samples, respectively. Comparing with the as-built sample, one can found that the transition hysteresis of the annealed NiTi–Nb alloy increases significantly, and is basically equivalent to that of the as-cast sample.

3.3. Compressive properties

Fig. 7 (a) shows the stress-strain curves of different specimens including the as-built and annealed NiTi–Nb samples made by LPBF, the cast $Ni_{50}Ti_{50}$ [47], the as-cast NiTi-Nb [47], a dense bulk NiTi prepared by LPBF [48], and Ni-rich NiTi prepared by LPBF [49]. Table 2 summarizes the corresponding yield strength ($\sigma_{0.2}$), ultimate compressive strength (UCS), and maximum strain (MS%) for these materials [47–49]. As observed from Table 2, the yield strength of the as-cast sample is 965 MPa, and the ultimate compressive stress reaches 1795 MPa when the strain is around 22%. Different from the as-built sample, the annealed sample shows a significant plateau region after elastic deformation at 250–300 MPa. The yield strength of the annealed sample is 1640 MPa, and the maximum compressive strength is 2384 MPa at strain of 39%. The yield strength, maximum stress, and strain of the as-built sample are close to or lower than the other samples reported in literature (as listed in Table 2). The annealed NiTi–Nb exhibits comparable or even higher mechanical properties compared to others reported in literature (Fig. 7 (e)), as expected from the strengthening effect of the submicron Nb precipitates within the NiTi-rich phase.

Fig. 7 (b) shows the stress–strain curves for the as-built and the annealed NiTi–Nb sample manufactured by LPBF. The residual strain (ε_R), superelastic strain (ε_{SE}), and pure elastic strain (ε_E) of the as-built and annealed samples are listed in Table 3. The annealed sample exhibits a stress platform at a compressive stress of 260 MPa (Fig. 7 (b)), indicating the beginning of martensitic transformation. This phenomenon was also observed previously in Ref. [50]. Subsequently, the strain linearly decreases to 10.6%, and superelastic recovery begins to occur when the sample is unloaded at 1700 MPa. After unloading, the residual plastic strain is 8.4%. The recovered strain (8.2%) during unloading is the sum of the elastic strain (5.6%) and the hyperelastic strain (2.6%). As shown in Fig. 7 (b), the annealed sample exhibits a significant stress plateau during loading and superelastic recovery during unloading.

The stress-strain curves of the as-built and the annealed samples after loading-unloading are shown in Fig. 7 (c)–(d). For the LPBF-produced NiTi–Nb eutectic-type alloy, residual plastic strain begins to accumulate in each successive loading-unloading cycle from the previous cycle. High superelastic recovery and elastic recovery are due to greater formation of martensites during deformation. The smaller residual strain during unloading reveals the de-twinning of martensite [8]. As shown in Fig. 7 (c) and (d), the superelasticity of the as-built sample is superior to that of the annealed sample, which indicates that the as-built sample has better de-twinning recovery. The annealed sample is strengthened by plasticity in the next cycle, and the cumulative residual strain indicates that the annealed sample has irreversible plastic deformation [8]. Fig. 7 (f) shows the strain of superelastic recovery and elastic recovery after unloading. The elasticities of the as-built sample and the annealed sample are 6.27% and 6.37%, respectively, for a maximum compressive strain of 21%. After cyclic compression for the annealed samples, the superelastic recovery and residual strain are 2.6% and 12%, respectively, which are greater than those in the as-built samples.

3.4. Microstructure evolution after deformation

Fig. 8 displays the microstructures of the NiTi-rich phase and the β-Nb phase in the annealed sample after compression. The SAED patterns of NiTi and Nb are shown in Fig. 8 (a) and Fig. 8 (b) insets, respectively. The β-Nb phases substantially surround the NiTi-rich phases, and a magnified view is shown in Fig. 8 (b). Similar results were reported in Refs. [30]. The NiTi matrix is about 20 μm in size, which is significantly larger than the NiTi-rich phase (300–500 nm), as indicated in Fig. 8 (a).

In addition, TEM images shown in Fig. 8 (b) and (c) reveal evident cracks and dislocations. Cracks in the β-Nb phase are accompanied by many dislocations slip around the β-Nb phase. As indicated by the black ellipse, the boundaries of precipitated β-Nb phase act as initiation sites for dislocations. Fig. 8 (d) shows a large number of tangled dislocations and stacking faults, tending to accumulate around the β-Nb phase. Additionally, martensitic laths are clearly seen in Fig. 8 (e). As shown in Fig. 8 (f), dislocations and stacking faults occur at the interface between the β-Nb phase and the eutectic phase.

Fig. 9 shows the microstructure evolution around the precipitated β-Nb in the annealed sample. There are stacking faults and martensite around two rod-like β-Nb particles (Fig. 9 (a)). Fig. 9 (b)–(c) show some lamellar high-density martensitic twins, which are of (001) compound type [8]. The corresponding SAED pattern (Fig. 9 (b)) confirms that the martensite is de-twinning ⟨011⟩ type II twin martensite [3]. The high-density dislocations accelerate geometric constraints and induce (001) matrix composite twin martensite transformation. The HRTEM images in Fig. 9 (d)–(f) show some lattice defects in the parallel (001) compound twin bands, and severe lattice distortions are also observed in Fig. 9 (d). Based on Ref. [51], the twins observed in Fig. 9 (e) are considered as twin martensite because the twins apparently exhibit high-density dislocations and stacking faults (Fig. 9 (e)). Dislocations and stacking faults accelerate lattice distortion during deformation, resulting in a large number of lattice defects in the matrix, which means that stacking faults and dislocation activities play a major role in lattice deformation.

Fig. 10 shows the results of micropillar compression on the Nb

Table 1
Phase transformation temperatures determined from the DSC curves for the as-built NiTi–Nb sample manufactured by LPBF, its annealed counterpart, and the as-cast NiTi–Nb alloy.

Samples	M_s (°C)	M_f (°C)	M_p (°C)	A_s (°C)	A_f (°C)	A_p (°C)	A_s–M_s (°C)
As-built	14.6	−20.1	11.3	−1.3	50.9	45.4	−15.9
Annealed	−47.4	−98.5	−81.3	−27.2	9.0	−10.1	29.6
As-cast	−29.6	−111.9	−113.6	−0.6	32.0	28.9	29

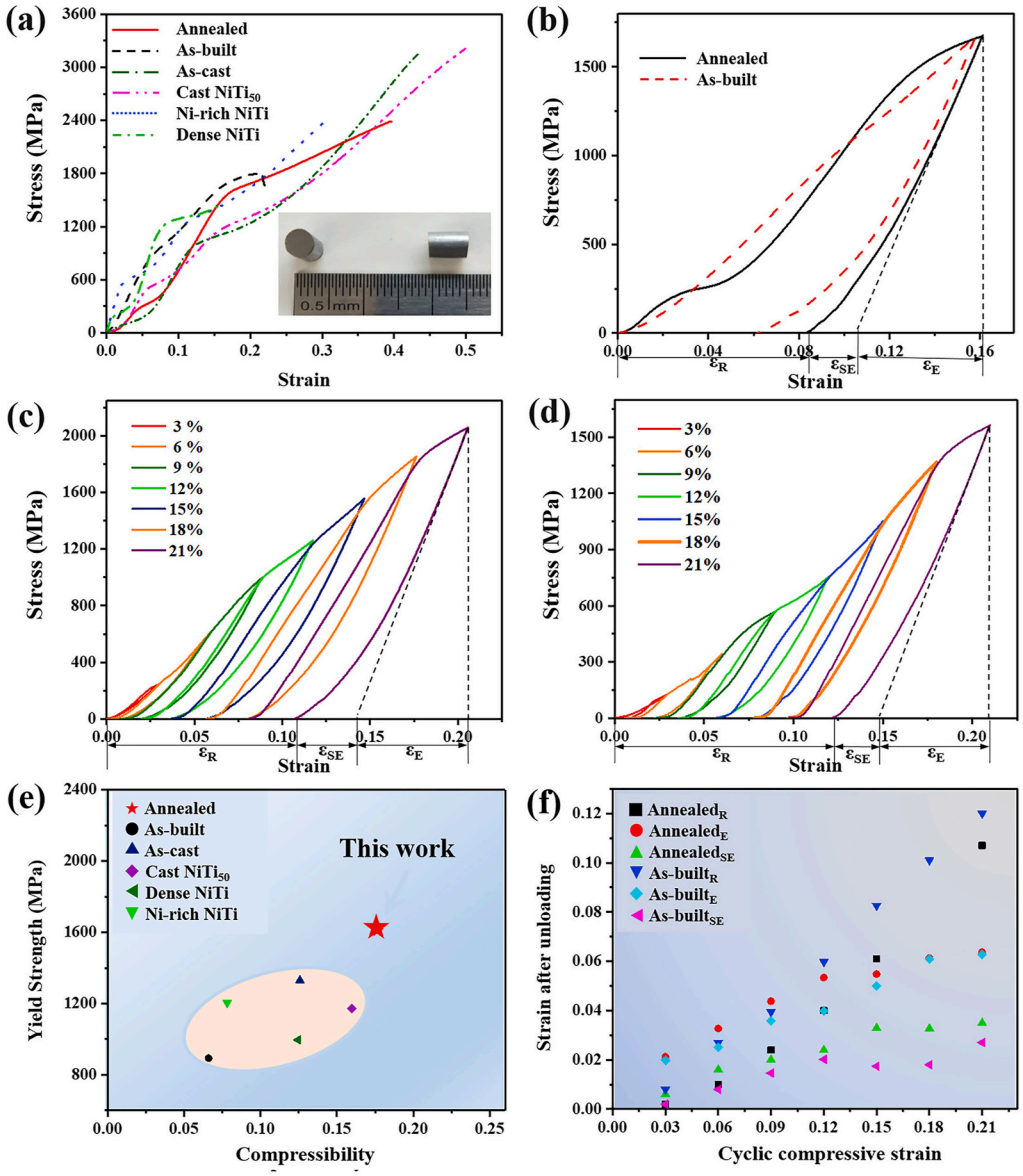

Fig. 7. (a) Stress-strain curves and (b) stress-strain curves of load-unload testing of various NiTi and NiTi–Nb alloys, cyclic compressive stress-strain curves of (c) the as-built samples manufactured by LPBF and (d) the annealed samples manufactured by LPBF, (e) relationship between yield strength and strain of various NiTi and NiTi–Nb, (f) comparison of strain after unloading. $Annealed_{SE}$: superelastic recovery of annealed; $Annealed_{E}$, elastic recovery of annealed; $Annealed_{R}$: residual strain of annealed. $As\text{-}built_{SE}$, $As\text{-}built_{E}$, and $As\text{-}built_{R}$ are the respective values of the As-built samples.

Table 2
Comparison of the mechanical properties of the as-built and annealed samples manufactured by LPBF and other NiTi and NiTi–Nb alloys produced by LPBF.

Compression	$\sigma_{0.2}$ (MPa)	UCS (MPa)	MS (%)
as-built	965	1795	22
Annealed	1640	2384	39
as-cast	960	3155	43
cast $Ni_{50}Ti_{50}$	1160	3211	50
Ni-rich NiTi	960	2410	30
dense NiTi	802	1440	16

Table 3
Comparison of cyclic compression properties of as-built and annealed NiTi–Nb alloys prepared by LPBF.

Loading-unloading	ε_R (%)	ε_{SE} (%)	ε_E (%)
as-built	6.2	4.0	5.5
Annealed	8.4	2.6	5.6

particle phase and eutectic phase, respectively, to clarify the specific mechanical properties of the different phases. The corresponding stress-strain curves of Nb particle and eutectic phases are shown in Fig. 10 (a). To compare the macroscopic compression tests and to avoid the effect of different micropillar size, the load-displacement data were converted into corresponding stress-strain curves. Fig. 10 (b) and (d) respectively show the morphologies of Nb particle and eutectic pillars before compression, and the morphology of the micropillar after unloading are respectively shown in Fig. 10 (c) and (e). Different from the slip band observed at the bottom of the Nb micropillar (Fig. 10 (e)), the eutectic micropillar shows evident upsetting and no slip band is observed after compression, proving that the eutectic micropillar has better toughness than the Nb pillar.

Nb particles and eutectic phase show a significantly different variation trend after initial line elastic loading. The Nb particle curve seems to fluctuate dramatically at a compressive stress of about 300 MPa, with a slip band appearing in the micropillar. With increasing elapsed time, the slip bands begin to accumulate, as shown in Fig. 10 (f)–(i). At the early stage, when the stress is applied to 500–750 MPa, the compression curve of the eutectic alloy fluctuates significantly (Fig. 10 (a)). Referring to the Nb pillar curve, the reason for the fluctuation of the eutectic pillar curve

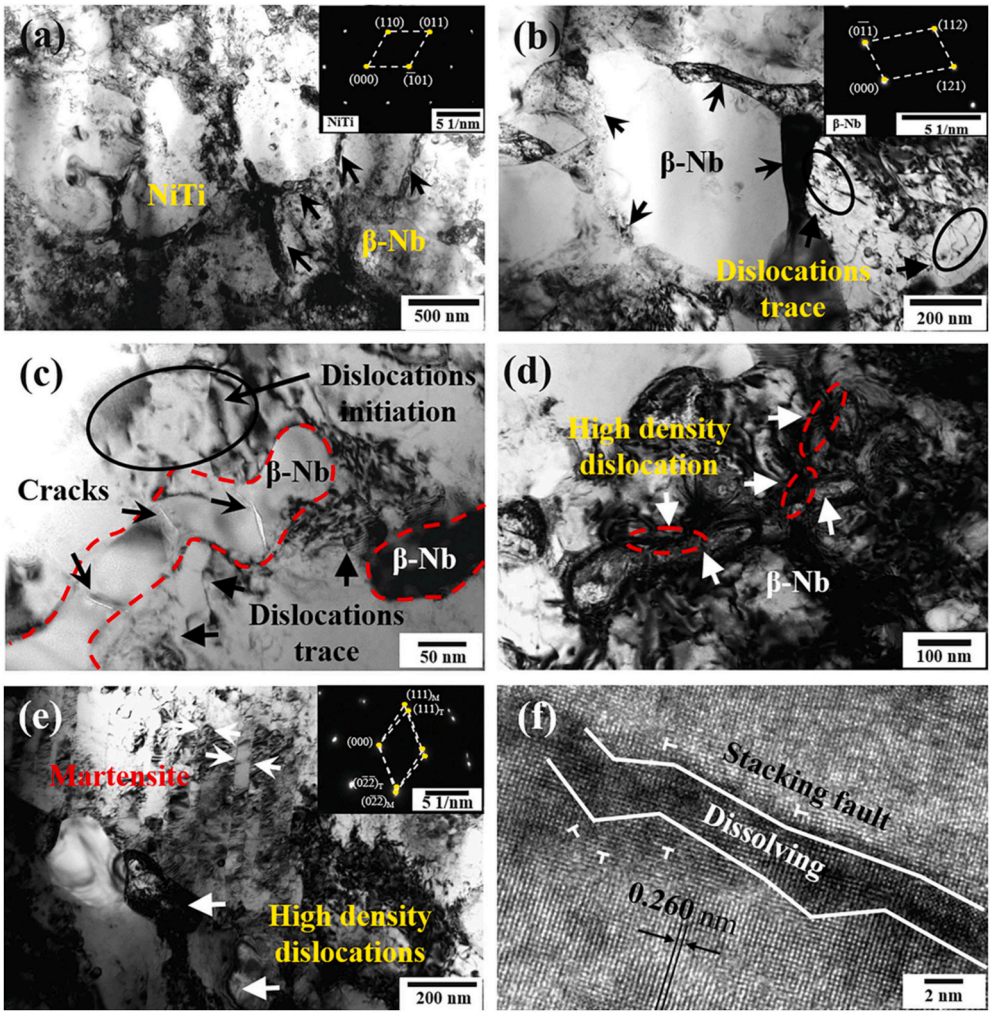

Fig. 8. TEM images of the annealed NiTi–Nb sample after compression: (a) β-Nb phase at the NiTi boundaries, (b) magnified view of β-Nb phase, (c) cracks and dislocations, (d) high-density dislocations around β-Nb, (e) dislocation structure and martensite, (f) HRTEM image of the coherent interface region.

is attributed to the occurrence of slip bands [52]. Because of the low amount of slip bands, the slip bands are not observed in the image. The stress-strain curve basically displays a linear growth after significant fluctuation of the curve. After that, the upward trend of the curve is lowered down significantly, and then returns to the initial growth trend. The final stage is the stress-strain curve of the unloading process. As the stress increases, the light-color submicron β-Nb phases are gradually extruded to the surface of the eutectic micropillar, as shown in Fig. 10 (j)–(m). The micropillar side surface becomes uneven due to the separation of the eutectic phase from the NiTi matrix during micropillar compression. No evident slip bands are observed in the eutectic micropillar throughout the entire compression process. Considering the effect of size effect, the stress applied to the micropillars would be higher than that applied by traditional millimeter-scale sample test [52].

After the compression, the eutectic microstructure and the martensite of the eutectic micropillar can be observed by TEM after FIB milling of the micropillars. Fig. 11 (a) shows the morphology of the thin region of FIB-milled TEM sample, and the inset presents a thin area of 4 μm in length and 2.5 μm in width. As seen from Fig. 11 (a)–(c), compound and lath martensites are evident around the β-Nb precipitates. As shown in Figs. 11 (c), $1^{\#}$ and $2^{\#}$ β-Nb are β-Nb precipitates with different thicknesses of NiTi attached, among which the NiTi attached to $1^{\#}$ is significantly more than $2^{\#}$ The surfaces of the two β-Nb precipitation phases show unequal initiation sites for dislocations due to the different thicknesses of the attached NiTi. As shown in the enlarged view of the β-Nb precipitation phase boundary on $2^{\#}$ β-Nb (Fig. 11 (d)), the deformation of the phase interface under stress loading has stacking faults and coherent crystal planes in different directions.

4. Discussions

4.1. Microstructure evolution

In the NiTi–Nb pseudo binary eutectic system, $Ni_{38}Ti_{36}Nb_{26}$ is a well-characterized eutectic point component. Based on the characteristics of laser powder bed fusion and rapid solidification, incompletely melted Nb particles are retained, resulting in an element diffusion trend around Nb particles [21]. According to Ref. [8], 10 at.% Nb can be dissolved into NiTi phase at the eutectic temperature, with greater Nb addition leading to more β-Nb phase separation. In this work, the Nb content is 12 at.%, and excessive Nb could not dissolve into the eutectic region while retaining the grain morphology. The saturated eutectic region tends to precipitate Nb phase during the cooling process. Grummon et al. [40] described the existence of five binary compounds of $NiTi_2$, NiTi, Ni_3Ti, Ni_3Nb, and NiNb in Ni–Ti–Nb ternary alloy at 900 °C, and suggested a quasi-binary eutectic system exists between ordered NiTi and disordered β-(Nb, Ni, Ti) solid solution [8].

The morphology of non-cluster eutectic phase obtained in annealed samples is significantly different from that of traditional as-cast samples prepared with the same composition. The optical microscopy images of

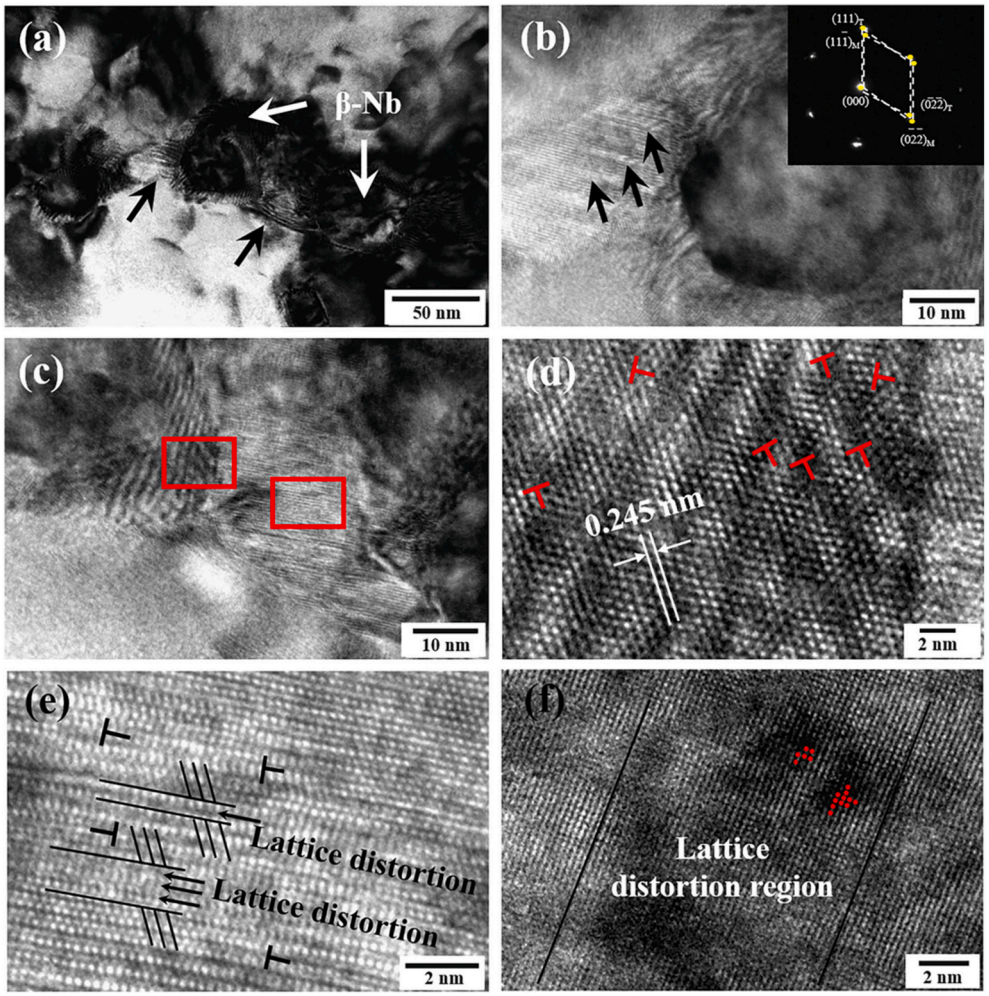

Fig. 9. Microstructure evolution near the precipitated β-Nb in annealed sample: (a) the microstructure around β-Nb, (b)–(c) magnified areas of (a), (d)–(e) HRTEM of areas indicated by red rectangles in (c), which shows (001) matrix compound twinned martensite, (f) lattice distortion region of NiTi–Nb. (For interpretation of the references to color in this figure legend, the reader is referred to the Web version of this article.)

the XY cross-section (Fig. 3 (e) and XZ cross-section (f)), columnar grains with ~10 μm in width and ~40 μm in length are observed in the center of the laser path, together with smaller equiaxed grains (200 nm - 2 μm). Comparing this result with the microstructure of the as-cast counterpart with the same composition [47], the material prepared herein by LPBF displays smaller equiaxed grains. The grain refinement efficiency of NiTi–Nb alloy prepared by LPBF is attributed to the high concentration of retained Nb particles, and the gradient concentration of retained Nb particles promotes the formation of β-Nb precipitation phase and eutectic phase. The continuous precipitation of Nb elements leads to the formation of a large supercooled region in front of the solid-liquid interface. An excessive region of supercooling can effectively offset the negative effects of high temperature gradients, which ensures that heterogeneous nucleation event waves are triggered in the component subcooling zone to achieve a columnar-to-equiaxed transition [33].

The atomic interaction force on the surface of adjacent atoms decreases as the crystal plane spacing increases, as does the misfit energy at the crystal interface. In the solid phase transformation, the change of crystal structure would cause the phase interface. For α and β two solid solutions (where α is the parent phase and β is the new phase), the α/β phase interface is formed where these phases contact each other. The degree of lattice misfit δ is defined as [53]:

$$\Delta = 2(\alpha_\beta - \alpha_\alpha) / (\alpha_\alpha + \alpha_\beta) \quad (1)$$

where, α_α and α_β are the lattice constants of α and β phases at the phase interface, respectively.

High-resolution morphology of the phase interface in Fig. 5 (c) reveals that the lattice fringes near the two-phase interface are parallel. Using Eq. (1), the misfit degree along the (111) direction of the two-phase coherence is 1.8%. When the two-phase interface intersects, both the lattice strain and the strain energy decrease and the interface bonding strength increases [54]. The difference in lattice constant between β-Nb and NiTi matrix causes lattice strain. As seen from Fig. 5 (c), there is relatively uniform contrast between the matrix side and the Nb-rich side fringe, and the central region exhibits severe lattice distortion. To reduce the strain caused by lattice misfit, the interface would generate misfit dislocations (Fig. 5 (d)) to absorb misfit on both sides of the phase interface. Thus, the two-phase interface is a semi-coherent interface. For the semi-coherent interface model, except for the severe distortion of the structure near the dislocation center, other positions can be considered to match exactly. The orientation relationship of the NiTi–Nb eutectic phase is $(100)_{\beta\text{-Nb}}//(011)_{B2}$ and $[01\bar{1}]_{\beta\text{-Nb}}//[01\bar{1}]_{B2}$. Reduction in the phase transition resistance lowers the free energy of the system. The lattice misfit of the eutectic phase interface satisfies the structure of the semi-coherent interface, so the dislocations at the interface significantly reduces the interface energy.

4.2. *Effect of β-Nb on strengthening mechanisms*

In this work, a high-strength NiTi–Nb alloy is developed specifically

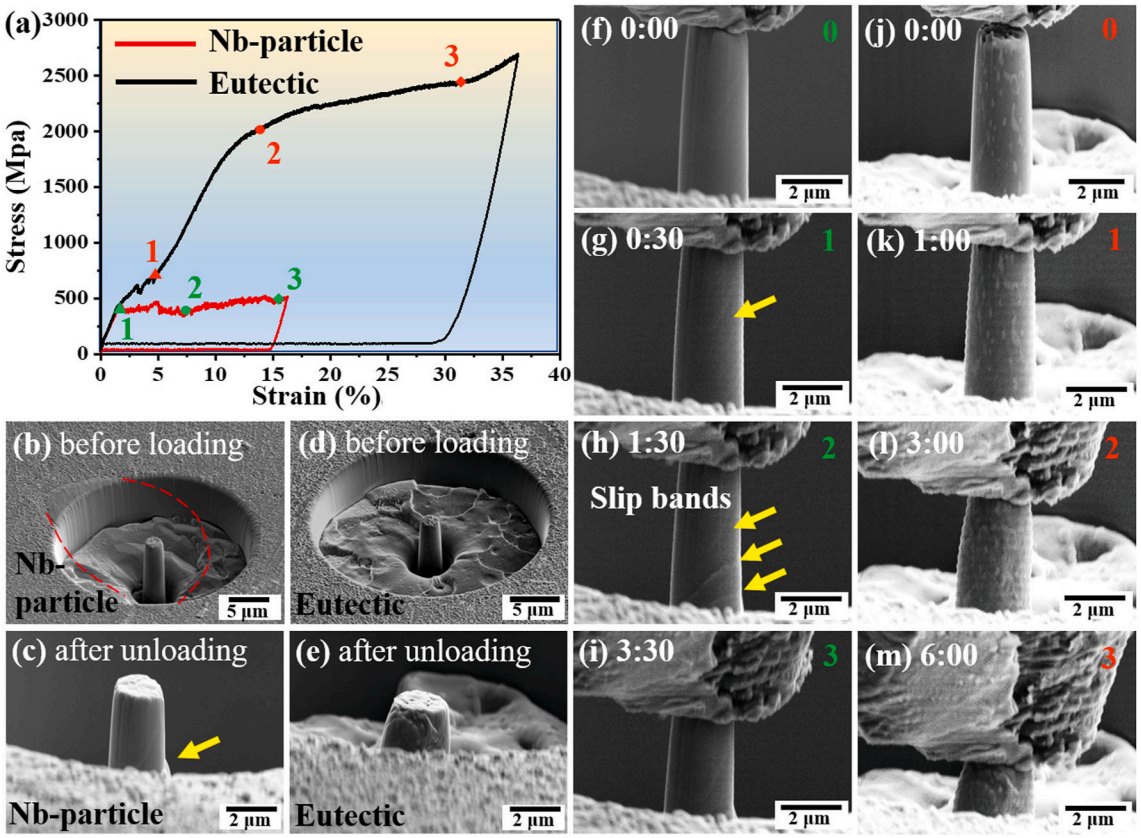

Fig. 10. In situ micropillar compression tests of the annealed NiTi–Nb: (a) Stress−strain curves of Nb particle and eutectic phases, (b–c) SEM images of Nb particle and eutectic phases before loading, (d–e) SEM images of Nb particle and eutectic phases after unloading, (f–i) SEM images of Nb particle phase at 0:00, 0:30, 1:30, and 3:30 during compression, (j–m) SEM images of eutectic phase at 0:00, 1:00, 3:00, and 6:00 during compression. The corresponding stress-strain relationships are indicated by numbers in (a). See supplementary videos SV1-SV2 for details.

for LPBF applications. After annealing at 850 °C, the yield strength of the material is as high as 1600 MPa (Fig. 7 (a)). It is believed that the main strengthening mechanisms should be attributed to the combined effect of Nb rich precipitation and eutectic structure.

During the high-speed solidification process of LPBF, an ultra-conventional amount of Nb is added to the solid solution (Fig. 3 (a)). Compared with the NiTi atoms present in the matrix, the atomic size and shear modulus of Nb atoms are very different, and these differences may generate local strain fields. The interaction between lattice distortion and dislocation restricts dislocation motion, thereby enhancing the yield strength of the material during deformation [55,56]. In current alloy systems, modulus hardening is considered as the main strengthening mechanism, and this hinders the motion of dislocations due to the difference in modulus values between the Nb-rich precipitates and the surrounding NiTi matrix [46].

As reported previously [33], an enhanced phase can significantly promote load transfer and achieve a toughening effect. The Nb phase exists as an enhanced phase, which enhances the strength of the alloy under stress loading. Since the Nb phase acts as a pinning point to prevent dislocation extension, it interweaves and piles up to the right of the β-Nb phase. The β-Nb precipitates can interact with dislocations to prevent the dislocations from moving freely, thereby increasing the yield strength of the material during deformation. Annealing can eliminate the residual stress caused by the temperature gradient generated during solidification and cooling of the sample preparation, thereby significantly improving the mechanical properties of the sample. The annealed sample exhibits a high yield strength and maximum compressive strength (Fig. 7 (a)). In addition, a distinct martensitic yielding stress platform at about 250–300 MPa (Fig. 7 (a) and (b)) is observed. As the stress increases, martensite reorientation takes place when the stress exceeds the martensitic yield stress. The Nb-rich phase (Fig. 4 (b)–(d)) has a Nb content exceeding 90 at.%, deviating from the eutectic composition. This indicates that a greater precipitation hardening effect can be obtained as a result of optimized annealing treatment, thereby further enhancing the compressive strength. Additionally, the submicron β-Nb phase exists as a soft phase surrounding the NiTi-rich phase, which can promote load transfer under stress loading, leading to higher stress and strain [56]. Annealing can also improve the segregation of β-Nb phase in NiTi–Nb alloy and dissolve the brittle precipitate formed during the LPBF process. As discussed in previous studies [16,35], the reduction in brittle precipitates and the increase in the β-Nb phase promote plastic deformation in grains.

4.3. Contribution of eutectic to mechanical properties

The high cooling rate in the LPBF process promotes the rapid diffusion of Nb in the NiTi matrix and may produce very fine eutectic microstructures, which enhances the strength and ductility of the LPBF-produced samples [56]. The high cooling rate can limit the diffusion of atoms and inhibit the eutectic coupling growth, leading to the formation of martensite [57]. Therefore, the formation of the needle-shaped martensite plates (Fig. 8 (f)) is attributed to the high cooling rate of the NiTi–Nb alloy manufactured by LPBF.

However, due to the extremely fine scale of the microstructure (including eutectic phase and highly condensed nanoscale precipitates), local stress concentration during mechanical deformation can be reduced, which would reduce the risk of crack initiation and ductility. At the same time, the deformation adaptation between coarse columnar grain regions and fine equiaxed grain regions also contributes to the ductility of developed alloys [58]. As mentioned above, the grain size of

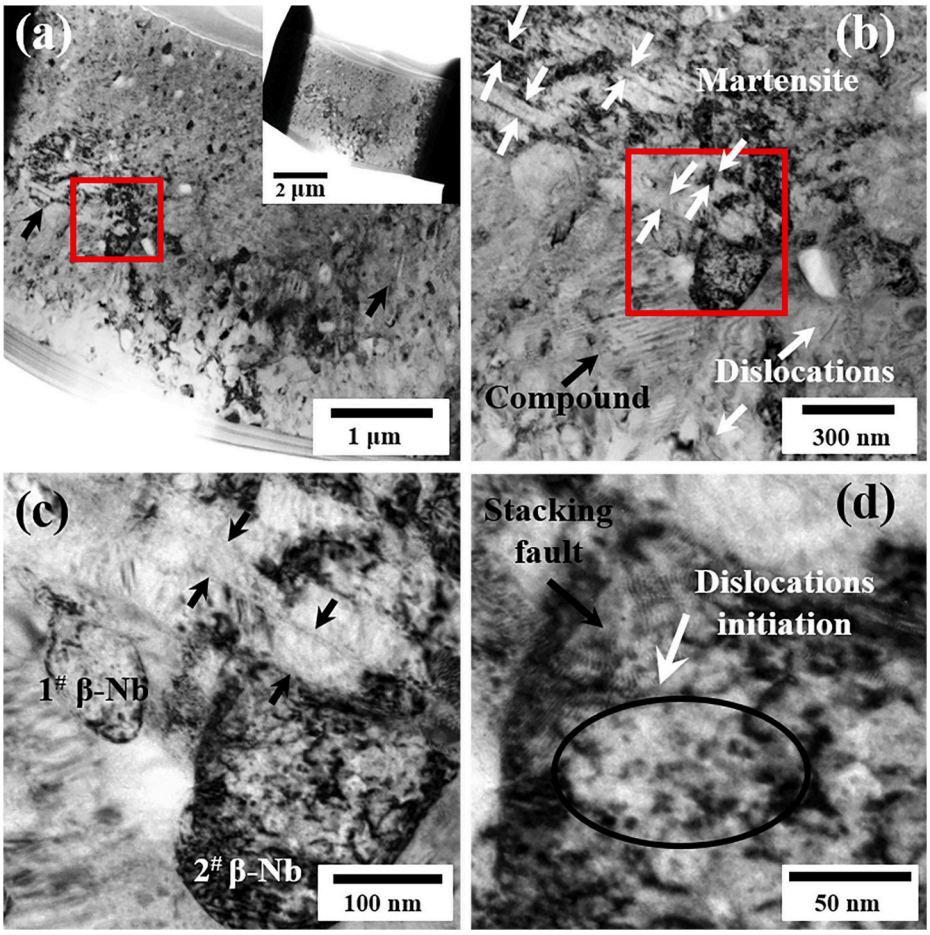

Fig. 11. TEM images of (a) the eutectic micropillar, (b) martensite and compound, (c) enlarged image of part indicated in (b), (d) stacking fault on Nb-rich boundaries.

NiTi–Nb alloy is refined due to the combined action of the primary eutectic phase and the submicron Nb-rich precipitated phase.

The micropillar compression experiments with low strength Nb particles show that, compared with eutectic pillar, β-Nb cracks appear first under the same loading condition (Fig. 10 (c)). Additionally, the uniform eutectic phase has higher strength than the Nb micropillar. With extrusion of the rod-shaped eutectic phase under loading, the stress-strain curve of eutectic micropillar tends to show a curve platform similar to that of the macroscopic annealed sample. In the high-resolution TEM results after micropillar compression, the atomic distances of the β-Nb precipitated phase and the phase near the NiTi matrix phase are 0.192 nm and 0.170 nm, respectively. Using Eq. (1), the misfit of the two-phase lattice interface can be calculated as 12.15%. It is clear that the characteristics of high strength of the NiTi–Nb eutectic-type alloy are mainly determined by uniform eutectic phases. Compared with traditional casting methods, the mechanical properties of NiTi–Nb eutectic alloys prepared by LPBF with ultrafine eutectic phase and precipitated Nb-rich phase show excellent combination of yield strength and plasticity.

5. Conclusions

In this work, NiTi–Nb eutectic-type alloy was fabricated by laser powder bed fusion using a mixture of spherical pre-alloyed NiTi powder and irregular small-particle Nb powder. The main results are summarized as follows.

(1) The composition of $Ni_{44}Ti_{44}Nb_{12}$ alloy is prepared according to the quasi-binary eutectic phase diagram and the ternary phase diagram. The morphology of the sample prepared by LPBF consists of staggered tracks and fish scale stacking faults and the microstructure is a uniform eutectic phase region, with a large amount of β-Nb precipitate phase. Columnar grains and fine equiaxed grains appear at the center and boundary, respectively, of the laser scanning path.

(2) Nb particles retained by LPBF promote the diffusion of Nb element and accelerate the eutectic phase transition and the precipitation of the β-Nb phases. The orientation relationship of the NiTi–Nb eutectic is $(100)_{\beta\text{-Nb}}//(011)_{B2}$ and $[01\bar{1}]_{\beta\text{-Nb}}//[01\bar{1}]_{B2}$. The precipitated β-Nb phases cause the surrounding dislocations to initiate, while interweave, and pile up and the dislocations and stacking faults at the boundary between the Nb-rich phase and the NiTi-rich phase promote the formation and phase transformation of martensite. The annealed samples undergo a more pronounced martensitic transformation, exhibiting a stress platform at 300 MPa.

(3) Micropillar compression confirmed that the eutectic pillar has a high strength of 2500 MPa and a compressive strain of 35%, making an important contribution to high strength. In comparison to other materials, the annealed NiTi–Nb eutectic-type alloy prepared by LPBF exhibits excellent compression properties: yield strength of 1640 MPa, compressive strength of 2384 MPa, and compressive strain of 39%. The demonstrated high strength suggests future directions for the design of high strength NiTi–Nb alloys.

(4) The characteristics of high strength of the NiTi–Nb eutectic-type alloy are mainly determined by uniform eutectic phases. Compared with traditional casting methods, the mechanical properties of NiTi–Nb eutectic alloys prepared by LPBF with ultrafine eutectic phase and precipitated Nb-rich phase show excellent combination of yield strength and plasticity.

Declaration of competing interest

The authors declare that they have no known competing financial interests or personal relationships that could have appeared to influence the work reported in this paper.

Acknowledgements

This research was funded by the National Natural Science Foundation of China (No. 51674167, No.51831011, No.51671152, No.51874225). Ling Zhang wishes to thank the financial support of the National Key Research and Development Program of China (Grant No. 2016YFB0700403) and Project No. 2020CDJDPT001 supported by the Fundamental Research Funds for the Central Universities. High-level Innovation team and Outstanding Scholars Program of Colleges and Universities in Guangxi: Innovative team of basic and Clinical Comprehensive Research on Bone and Joint Degenerative Diseases. Liqiang Wang also thanks Wei Liu from Xi'an University of Architecture and Technology for analyzing the experimental data.

Appendix A. Supplementary data

Supplementary data to this article can be found online at https://doi.org/10.1016/j.compositesb.2020.108358.

References

[1] Zhang L, Chen L. A review on biomedical titanium alloys: recent progress and prospect. Adv Eng Mater 2019;21(4):1801215.
[2] Lee J-H, Lee K-J, Choi E. Flexural capacity and crack-closing performance of NiTi and NiTiNb shape-memory alloy fibers randomly distributed in mortar beams. Compos B Eng 2018;153:264–76.
[3] Wang L, Wang C, Dunand DC. Microstructure and strength of NiTi-Nb eutectic braze joining NiTi wires. Metall Mater Trans 2015;46(4):1433–6.
[4] Wang L, Wang C, Zhang LC, Chen L, Lu W, Zhang D. Phase transformation and deformation behavior of NiTi-Nb eutectic joined NiTi wires. Sci Rep 2016;6:23905.
[5] Zhai W, Zhu Z, Zhou W, Nai SML, Wei J. Selective laser melting of dispersed TiC particles strengthened 316L stainless steel. Compos B Eng 2020;199:108291.
[6] AlMangour B, Yang J-M. Understanding the deformation behavior of 17-4 precipitate hardenable stainless steel produced by direct metal laser sintering using micropillar compression and TEM. Int J Adv Manuf Technol 2016;86:1–4.
[7] Wang L, Wang C, Lu W, Zhang D. Superelasticity of NiTi–Nb metallurgical bonding via nanoindentation observation. Mater Lett 2015;161:255–8.
[8] Wang L, Xie L, Zhang L-C, Chen L, Ding Z, Lv Y, et al. Microstructure evolution and superelasticity of layer-like NiTiNb porous metal prepared by eutectic reaction. Acta Mater 2018;143:214–26.
[9] Zhang L-C, Chen L-Y, Wang LQ. Surface modification of titanium and titanium alloys: technologies, developments, and future interests. Adv Eng Mater 2020;22:1901258.
[10] Liu W, Liu SF, Wang LQ. Surface modification of biomedical titanium alloy: micromorphology, microstructure evolution and biomedical applications. Coatings 2019;9:249.
[11] Wang Q, Zhou P, Liu S, Attarilar S, Ma RL-W, Zhong Y, et al. Multi-scale surface treatments of titanium implants for rapid osseointegration: A Review. Nanomaterials 2020;10(6):1244.
[12] Fan QC, Zhang Y, Zhang YH, Wang YY, Yan EH, Huang SK, et al. Influence of Ni/Ti ratio and Nb addition on martensite transformation behavior of NiTiNb alloys. J Alloys Compd 2019;790:1167–76.
[13] Wang L, Xie L, Lv Y, Zhang L-C, Chen L, Meng Q, et al. Microstructure evolution and superelastic behavior in Ti-35Nb-2Ta-3Zr alloy processed by friction stir processing. Acta Mater 2017;131:499–510.
[14] Liu S, Liu J, Wang L, Ma RL-W, Zhong Y, Lu W, et al. Superelastic behavior of in-situ eutectic-reaction manufactured high strength 3D porous NiTi-Nb scaffold. Scripta Mater 2020;181:121–6.
[15] Ying C, Hai-chang J, Li-jian R, Li X, Xin-qing Z. Mechanical behavior in NiTiNb shape memory alloys with low Nb content. Intermetallics 2011;19(2):217–20.
[16] Shu XY, Lu SQ, Li GF, Liu JW, Peng P. Nb solution influencing on phase transformation temperature of $Ni_{47}Ti_{44}Nb_9$ alloy. J Alloys Compd 2014;609:156–61.
[17] Huang S, Sing SL, Looze Gd, Wilson R, Yeong WY. Laser powder bed fusion of titanium-tantalum alloys: compositions and designs for biomedical applications. J. Mechan. Behav. Biomed. Mater. 2020;108:103775.
[18] AlMangour B, Grzesiak D, Borkar T, Yang J-M. Densification behavior, microstructural evolution, and mechanical properties of TiC/316L stainless steel nanocomposites fabricated by selective laser melting. Mater Des 2018;138:119–28.
[19] Sing SL, Huang S, Yeong WY. Effect of solution heat treatment on microstructure and mechanical properties of laser powder bed fusion produced cobalt-28chromium-6molybdenum. Mater. Sci. Eng.: A 2020;769:138511.
[20] Ngo TD, Kashani A, Imbalzano G, Nguyen KTQ, Hui D. Additive manufacturing (3D printing): a review of materials, methods, applications and challenges. Compos B Eng 2018;143:172–96.
[21] Lewandowski JJ, Seifi M. Metal additive manufacturing: a review of mechanical properties. Annu Rev Mater Res 2016;46(1):151–86.
[22] AlMangour B, Yang J-M. Improving the surface quality and mechanical properties by shot-peening of 17-4 stainless steel fabricated by additive manufacturing. Mater Des 2016;110:914–24.
[23] AlMangour B, Grzesiak D, Yang J-M. Rapid fabrication of bulk-form TiB2/316L stainless steel nanocomposites with novel reinforcement architecture and improved performance by selective laser melting. J Alloys Compd 2016;680:480–93.
[24] Salmi A, Atzeni E. Residual stress analysis of thin AlSi10Mg parts produced by Laser Powder Bed Fusion. Virtual Phys Prototyp 2019;15(1):49–61.
[25] Wang P, Gammer C, Brenne F, Niendorf T, Eckert J, Scudino S. A heat treatable TiB2/Al-3.5Cu-1.5Mg-1Si composite fabricated by selective laser melting: microstructure, heat treatment and mechanical properties. Compos B Eng 2018;147:162–8.
[26] Hafeez N, Liu S, Lu E, Wang L, Liu R, lu W, et al. Mechanical behavior and phase transformation of β-type Ti-35Nb-2Ta-3Zr alloy fabricated by 3D-Printing. J Alloys Compd 2019;790:117–26.
[27] Hafeeza N, Liu J, Wang L, Wei D, Tang Y, Lu W, et al. Superelastic response of low-modulus porous beta-type Ti-35Nb-2Ta-3Zr alloy fabricated by laser powder bed fusion. Additive Manuf. 2020;34:101264.
[28] Yang Y, Zhan JB, Sun ZZ, Wang HL, Lin JX, Liu YJ, et al. Evolution of functional properties realized by increasing laser scanning speed for the selective laser melting fabricated NiTi alloy. J Alloys Compd 2019;804:220–9.
[29] Yang Y, Zhan JB, Li B, Lin JX, Gao JJ, Zhang ZQ, et al. Laser beam energy dependence of martensitic transformation in SLM fabricated NiTi shape memory alloy. Materialia 2019;6:100305.
[30] Elahinia M, Shayesteh Moghaddam N, Amerinatanzi A, Saedi S, Toker GP, Karaca H, et al. Additive manufacturing of NiTiHf high temperature shape memory alloy. Scripta Mater 2018;145:90–4.
[31] Saedi S, Turabi AS, Andani MT, Haberland C, Karaca H, Elahinia M. The influence of heat treatment on the thermomechanical response of Ni-rich NiTi alloys manufactured by selective laser melting. J Alloys Compd 2016;677(25):204–10.
[32] Wang JC, Liu YJ, Qin P, Liang SX, Sercombe TB, Zhang LC. Selective laser melting of Ti–35Nb composite from elemental powder mixture: microstructure, mechanical behavior and corrosion behavior. Mater. Sci. Eng.: A 2019;760:214–24.
[33] Zhang D, Qiu D, Gibson MA, Zheng Y, Fraser HL, StJohn DH, et al. Additive manufacturing of ultrafine-grained high-strength titanium alloys. Nature 2019;576(7785):91–5.
[34] Todaro CJ, Easton MA, Qiu D, Zhang D, Bermingham MJ, Lui EW, et al. Grain structure control during metal 3D printing by high-intensity ultrasound. Nat Commun 2020;11(1):142.
[35] Oliveira JP, Cavaleiro AJ, Schell N, Stark A, Miranda RM, Ocana JL, et al. Effects of laser processing on the transformation characteristics of NiTi: a contribute to additive manufacturing. Scripta Mater 2018;152:122–6.
[36] Fischer M, Joguet D, Robin G, Peltier L, Laheurte P. In situ elaboration of a binary Ti-26Nb alloy by selective laser melting of elemental titanium and niobium mixed powders. Mater Sci Eng C 2016;62:852–9.
[37] Kang N, Lin X, Coddet C, Wen X, Huang W. Selective laser melting of low modulus Ti-Mo alloy: α/β heterogeneous conchoidal structure. Mater Lett 2020;267:127544.
[38] Kang N, Coddet P, Chen C, Wang Y, Liao H, Coddet C. Microstructure and wear behavior of in-situ hypereutectic Al–high Si alloys produced by selective laser melting. Mater Des 2016;99:120–6.
[39] Kang N, Coddet P, Dembinski L, Liao H, Coddet C. Microstructure and strength analysis of eutectic Al-Si alloy in-situ manufactured using selective laser melting from elemental powder mixture. J Alloys Compd 2017;691:316–22.
[40] Grummon DS, Shaw JA, Foltz J. Fabrication of cellular shape memory alloy materials by reactive eutectic brazing using niobium. Materials Science and Engineering: A 2006;438–440:1113–8.
[41] Vora P, Mumtaz K, Todd I, Hopkinson N. AlSi12 in-situ alloy formation and residual stress reduction using anchorless selective laser melting. Additive Manuf. 2015;7:12–9.
[42] Kuo CN, Chua CK, Peng PC, Chen YW, Sing SL, Huang S, et al. Microstructure evolution and mechanical property response via 3D printing parameter development of Al–Sc alloy. Virtual Phys Prototyp 2020;15(1):120–9.
[43] Toker GP, Nematollahi M, Saghaian SE, Baghbaderani KS, Benafan O, Elahinia M, et al. Shape memory behavior of NiTiHf alloys fabricated by selective laser melting. Scripta Mater 2020;178:361–5.
[44] Papon EA, Haque A, Mulani SB. Process optimization and stochastic modeling of void contents and mechanical properties in additively manufactured composites. Compos B Eng 2019;177:107325.
[45] Jiang S, Liang Y, Zhang Y, Zhao Y, Zhao C. Influence of addition of Nb on phase transformation, microstructure and mechanical properties of equiatomic NiTi SMA. J Mater Eng Perform 2016;25(10):4341–51.

[46] AlMangoura B, Kimb Y-K, Grzesiakc D, Lee K-A. Novel TiB_2-reinforced 316L stainless steel nanocomposites with excellent room- and high-temperature yield strength developed by additive manufacturing. Compos B Eng 2019;159:51–63.
[47] Liu S, Han S, Wang L, Liu J, Tang H. Effects of Nb on the microstructure and compressive properties of an as-cast $Ni_{44}Ti_{44}Nb_{12}$ eutectic alloy. Materials 2019;12 (24):4118–26.
[48] Ravari MRK, Esfahani SN, Andani MT, Kadkhodaei M, Ghaei A, Karaca H, et al. On the effects of geometry, defects, and material asymmetry on the mechanical response of shape memory alloy cellular lattice structures. Smart Mater Struct 2016;25(2):025008.
[49] Haberland C, Meier H, Frenzel J. On the properties of Ni-rich NiTi shape memory parts produced by selective laser melting. In: Proceedings of the ASME 2012 Conference on Smart Materials, Adaptive Structures and Intelligent Systems. Georgia, USA: Stone Mountain; 2012.
[50] Wang M, Jiang M, Liao G, Guo S, Zhao X. Martensitic transformation involved mechanical behaviors and wide hysteresis of NiTiNb shape memory alloys. Prog Nat Sci: Mater Int 2012;22(2):130–8.
[51] Chen W, Zhang J, Cao S, Pan Y, Huang M, Hu Q, et al. Strong deformation anisotropies of ω-precipitates and strengthening mechanisms in Ti-10V-2Fe-3Al alloy micropillars: precipitates shearing vs precipitates disordering. Acta Mater 2016;117:68–80.
[52] Paccou E, Tanguy B, Legros M. Micropillar compression study of Fe-irradiated 304L steel. Scripta Mater 2019;172:56–60.
[53] Cui CJ, Xue T, Yang C, Yang M, Tian LL, Wen YG. The orientation relationship and latticemisfit of Ni-Si eutectic alloy by HRTEM. J Funct Mater 2016;8(47):8196–9.
[54] Kang N, Coddet P, Liu Q, Liao H, Coddet C. In-situ TiB/near α Ti matrix composites manufactured by selective laser melting. Additive Manuf 2016;11:1–6.
[55] Kang N, Ma W, Heraud L, El Mansori M, Li F, Liu M, et al. Selective laser melting of tungsten carbide reinforced maraging steel composite. Additive Manuf 2018;22: 104–10.
[56] Hu Y, Cong W, Wang X, Li Y, Ning F, Wang H. Laser deposition-additive manufacturing of TiB-Ti composites with novel three-dimensional quasi-continuous network microstructure: effects on strengthening and toughening. Compos B Eng 2018;133:91–100.
[57] Shuai C, Xue L, Gao C, Peng S, Zhao Z. Rod-like eutectic structure in biodegradable Zn–Al–Sn alloy exhibiting enhanced mechanical strength. ACS Biomater Sci Eng 2020;6(7):3821–31.
[58] Chen B, Kondoh K, Li JS, Qian M. Extraordinary reinforcing effect of carbon nanotubes in aluminium matrix composites assisted by in-situ alumina nanoparticles. Compos B Eng 2020;183:107691.